

Lateral Baroclinic Forcing Enhances Sediment Transport from Shallows to Channel in an Estuary

Jessica R. Lacy · Steve Gladding · Andreas Brand ·
Audric Collignon · Mark Stacey

Received: 25 January 2013 / Revised: 18 October 2013 / Accepted: 15 November 2013 / Published online: 15 January 2014
© Coastal and Estuarine Research Federation 2014

Abstract We investigate the dynamics governing exchange of sediment between estuarine shallows and the channel based on field measurements at eight stations spanning the interface between the channel and the extensive eastern shoals of South San Francisco Bay. The study site is characterized by longitudinally homogeneous bathymetry and a straight channel, with friction more important than the Coriolis forcing. Data were collected for 3 weeks in the winter and 4 weeks in the late summer of 2009, to capture a range of hydrologic and meteorologic conditions. The greatest sediment transport from shallows to channel occurred during a pair of strong, late-summer wind events, with westerly winds exceeding 10 m/s for more than 24 h. A combination of wind-driven barotropic return flow and lateral baroclinic circulation caused the transport. The lateral density

gradient was produced by differences in temperature and suspended sediment concentration (SSC). During the wind events, SSC-induced vertical density stratification limited turbulent mixing at slack tides in the shallows, increasing the potential for two-layer exchange. The temperature- and SSC-induced lateral density gradient was comparable in strength to salinity-induced gradients in South Bay produced by seasonal freshwater inflows, but shorter in duration. In the absence of a lateral density gradient, suspended sediment flux at the channel slope was directed towards the shallows, both in winter and during summer sea breeze conditions, indicating the importance of baroclinically driven exchange to supply of sediment from the shallows to the channel in South San Francisco Bay and systems with similar bathymetry.

Communicated by Carl T. Friedrichs

J. R. Lacy (✉)
Pacific Coastal and Marine Science Center, U.S. Geological
Survey, 400 Natural Bridges Drive, Santa Cruz, CA 95060, USA
e-mail: jlacy@usgs.gov

S. Gladding · A. Collignon · M. Stacey
Department of Civil and Environmental Engineering,
University of California, Berkeley, CA, USA

S. Gladding
e-mail: sgladding@gmail.com

A. Collignon
e-mail: acollignon@eng.ucsd.edu

M. Stacey
e-mail: mstacey@berkeley.edu

A. Brand
Department of Surface Waters, Swiss Federal Institute of Aquatic
Science and Technology (EAWAG), Kastanienbaum, Switzerland
e-mail: Andreas.Brand@eawag.ch

Keywords Sediment transport ·
Estuarine hydrodynamics · Lateral circulation ·
Baroclinic forcing · Estuarine shallows · San Francisco Bay

Introduction

Estuaries tend to retain fine sediments, and these sediments form an important component of several estuarine habitats, including subtidal and intertidal mudflats and marshes. The fine sediments are riverine in origin, and following their initial deposition in channels or shallows, they are typically resuspended and redistributed both within and between habitat types repeatedly, by a variety of processes. Redistribution between channels, shallows, and marshes is critical to the maintenance of estuarine habitats and is a critical part of an estuarine sediment budget, because it can result in very long (decades) sediment residence times.

In this paper, we investigate one component of this redistribution: sediment flux at a shoal–channel interface. The study is based on time-series measurements of velocity and suspended sediment concentration (SSC) collected in South San Francisco Bay (South Bay). South Bay is comprised of a 15-m deep channel flanked by broad subtidal flats with depths of 2–3 m relative to mean lower low water (MLLW) (Conomos et al. 1985) (Fig. 1). Freshwater inflows to South Bay are relatively low and are restricted to the wet winter season. The tidal range is 1.5 m, and tidal currents generate significant mixing (Walters 1982). Summer winds are also an important source of circulation and mixing, due to the shallow depth and long fetch.

Sediment is transported between shallows and channels by both advective and dispersive mechanisms. Cross-channel advective transport tends to be much less than

along-channel transport, because tidal currents in both channels and shallows are predominately parallel to the channel. Wind and lateral baroclinic forcing are two potentially important sources of cross-channel circulation and shoal–channel exchange. The Coriolis and centrifugal forcing, which are significant sources of transverse circulation in many estuaries, are negligible in South Bay, because the channel is fairly straight and the system is shallow (Valle-Levinson et al. 2003).

Spatial gradients in SSC in combination with oscillating currents at any timescale, such as turbulence, waves, or tides, are an important source of dispersive flux, transporting sediment towards regions of lower concentration (Friedrichs 2011). Dispersion associated with spatial SSC gradients is particularly important in regions of variable bathymetry, because changes in depth generally correspond

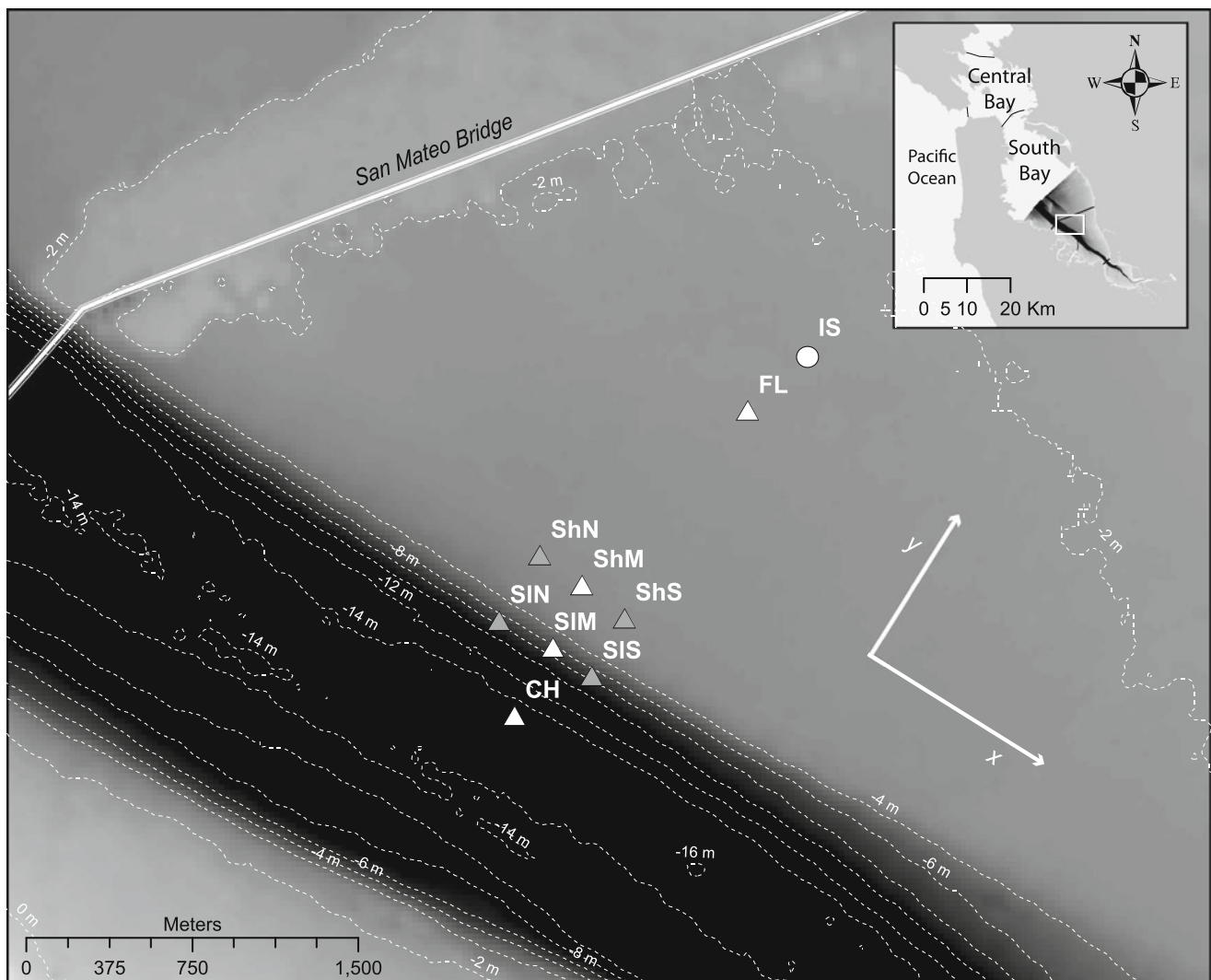


Fig. 1 Site map with station locations, bathymetric contours at 2-m intervals, and coordinate system. Symbols indicate type of data collected: time-series data (gray triangles), bed sediment grain size

(white circle), and both (white triangles). Bathymetric datum is mean lower low water. The white rectangle in inset map shows study site

to variations in bed shear stress. In a channel–shoal system, this mechanism can transport sediment from channel to shoal if, for example, tidally driven resuspension is greater in the channel than the shallows, or from shoal to channel, if wave-driven resuspension is greater in the shallows than in the channel. Dispersive suspended sediment flux (SSF) can also be generated by temporal variations in forcing; for example, increased wind-wave resuspension at low tide may result in landward SSF.

Despite its episodic nature and small magnitude compared to axial transport, lateral circulation and transport are critical not only to sediment redistribution, but to many other aspects of estuarine hydrodynamics and ecology. Lateral circulation and shoal–channel exchange have been shown to influence stratification, turbulence, along-channel momentum (Lacy et al. 2003; Lerczak and Geyer 2004), and along-channel SSF (Fugate et al. 2007), as well as phytoplankton dynamics (Huzzey et al. 1990; Thompson et al. 2008).

The paper addresses two questions: What conditions or mechanisms generate transport of sediment from the shallows to the channel, or the reverse? How do the magnitude and direction of SSF vary spatially and temporally in the channel–shoal system, and why? Most of the observed sediment flux from the shallows to the channel occurred during short, strong wind events, indicating the importance of episodic transport. We show that lateral baroclinic forcing played a critical role in shoal–channel sediment transport, both in the wet season and during dry conditions, when a lateral density gradient developed due to differences in temperature and SSC.

South San Francisco Bay

South Bay extends southeast from the Oakland Bay Bridge. Our study was conducted south of the San Mateo Bridge, at the interface between the channel and extensive eastern flats (Fig. 1). South Bay is well mixed much of the year. More than 90 % of the freshwater entering San Francisco Bay flows into the northern reach of the estuary, and in contrast, South Bay tributaries are relatively small and seasonal. Freshwater inflow produces a dynamically significant longitudinal salinity gradient only episodically, in the wet winter season.

Freshwater can influence circulation in South Bay by two pathways (Walters et al. 1985; Cheng and Gartner 1985). High flows into the northern estuary can depress salinities in Central Bay below those in South Bay, driving reverse estuarine circulation. Alternatively, freshwater inflows from local tributaries can lower salinities at the southern end of South Bay, generating classical estuarine circulation. This second mechanism tends to be more important to the south

of the San Mateo Bridge. As dry conditions return in the spring, salinities increase to near-oceanic levels through density-driven flow from the Pacific Ocean. When longitudinal salinity gradients and vertical stratification are present, lateral salinity gradients develop across the shoals of South Bay (Huzzey et al. 1990; Gross et al. 1999). Tidal currents in the channel of South Bay range up to approximately 1 m/s, with significant variation over the spring–neap tidal cycle (Cheng and Gartner 1985). Because of the strength of the tidal currents, the stratification that occurs in South Bay is typically intermittent, although it may persist for several days during neap tides (Lucas et al. 2009).

Summer winds in the region are typically from the west or northwest, with a strong daily sea breeze (Conomos et al. 1985). In winter, winds are light, except during storms, which are typically southeasterly and last 2–3 days. Wind-driven flows govern the subtidal circulation of South Bay in the dry season, with southeasterly flows over the shoals and return flows in the channel (Walters 1982; Cheng and Gartner 1985).

South Bay is characterized by fine-grained sediments and tends to be more turbid than the northern estuary. The spring–neap variation in tidal energy accounts for about half of the variability in suspended sediment concentrations in the South Bay channel, with SSC lagging tidal energy by approximately 2 days (Schoellhamer 1996). In the shallows, SSC depends more strongly on wind speed and direction than tidal energy, due to wind-wave resuspension (Schoellhamer 1996; Lacy et al. 1996; Brand et al. 2010). The short-period (typically 2–3 s) wind waves occurring in South Bay do not penetrate the depth of the channel, but pulses of SSC appear to reach the channel from the shoals during strong ebb tides. Schoellhamer (1996) attributed the spring–neap variability in SSC in the channel to a combination of greater local resuspension by tidal currents and greater connectivity with the shoals during spring tides.

Methods

Field Data Collection

Time-series data were collected at eight stations in four depth zones: channel, middle of the slope between channel and flats (slope); top of the slope between channel and flats (shoulder); and on the subtidal flats, 1.5 km from the channel edge (flats) (Table 1). There were two deployments to investigate seasonal variability: 24 Feb–16 Mar 2009 (winter), targeting the influence of freshwater inflows and winter storms, and 9 Sep–7 Oct 2009 (summer), intended to capture dry-season conditions and effects of the daily summer sea breeze.

Table 1 Locations and depths of stations

Name	ID	Longitude, E	Latitude, N.	Depth m MLLW
Channel	CH	122.22187	37.57397	15.2
Slope North	SIN	122.22263	37.57785	7.3
Slope Mid	SIM	122.21988	37.57673	6.5
Slope South	SIS	122.21790	37.57556	7.3
Shoulder North	ShN	122.22049	37.58053	2.6
Shoulder Mid	ShM	122.21835	37.57927	2.6
Shoulder South	ShS	122.21622	37.57788	2.6
Flats	FL	122.20977	37.58632	2.2
Inshore	IS	122.20670	37.58862	2.1

Instrumentation was essentially the same during the two deployments. The channel and slope stations were instrumented with bottom-mounted upward-looking acoustic Doppler current profilers (ADCP) and near-bed and near-surface conductivity, temperature, and depth sensors (CTD) with optical backscatter sensors (OBS). At the shoulder stations, one or two acoustic Doppler velocimeters (ADV), a CTD, and an OBS sampled within 1 m of the bed. A larger tripod was deployed at Flats, supporting two ADVs, two CTDs, two OBS, and a laser in situ scattering and transmissometry instrument (LISST), which measures concentration and grain size distribution of suspended sediment. Pressure sensors measured tidal stage and wave heights at all stations. Station locations, names, and depths are shown in Table 1 and Fig. 1, and instrument heights are listed in Table 2. The ADVs collected 8-min bursts at 8 or 10 Hz, hourly at Shoulder Mid and every 12 min at all other stations. The ADCPs sampled continuously at 1 Hz: 50-s averages every 12 min were extracted from the data for calculating SSF.

Both the velocity and SSC data used in calculating SSF were derived from acoustic velocimeters. The data sets from the velocimeters in Table 2 were complete, with the following exceptions. In winter, no velocity data were collected at Slope South or Shoulder Mid, due to instrument failure. In addition, the ADCP records at Channel and Slope Mid ended on 6 Mar, and the ADCP at Slope North collected data only during 2–16 Mar. During the summer deployment, the ADCP record at Channel ended on 30 Sep.

Bed sediments were collected with a Ponar grab sampler at Channel, Slope Mid, Shoulder Mid, Flats, and Inshore on 31 Oct 2008, and on 25 Feb, 4 Mar, 13 Mar, 16 Sep, and 28 Sep 2009 (Table 1, Fig. 1). Sampling was unsuccessful at Slope Mid on 28 Sep. Sediments from the top 2 cm of the sample were analyzed for grain size distribution using standard techniques. Sand (63 μm –2 mm) and fine fractions (<63 μm) were quantified in 1/4 ϕ size classes with a Beckman Coulter Model LS230 laser diffraction particle analyzer.

Table 2 Details of field deployment

ID	Instrument	Height of measurements
CH	ADCP	1.9 mab to surface at 0.5-m intervals
	CTD+OBS	0.4 mab
SIN	CTD+OBS	2 mbs
	ADCP	1.0 mab to surface at 0.25-m intervals
	CTD	0.5 mab
	OBS	0.2 mab
	CTD	0.75 mbs
	OBS	0.55 mbs
SIM	ADCP	1.5 mab to surface at 0.25 m intervals
	CTD	0.6 mab
	OBS	0.42 mab
	CTD	0.75 mbs
	OBS	0.6 mbs
	ADCP	1.2 mab to surface at 0.25-m intervals
SIS	CTD	0.5 mab
	OBS	0.3 mab
	CTD+OBS	1.0 mbs
	ADV	0.5 mab
	PCADP (summer)	2.0–3.3 mab at 0.1-m intervals
	CTD	0.65 mab
ShM	OBS	0.5 mab
	ADV	0.25 mab
	OBS	0.25 mab
	ADV	0.5 mab
ShS	CTD + OBS	0.46 mab
	ADV	(winter) 0.34 mab
	ADV	(summer) 0.25 mab
FL	OBS	(summer) 0.25 mab
	ADV+OBS	0.35 mab
	ADV+OBS	0.7 mab
	CTD	0.8 mab
	CTD	1.42 mab
	LISST	0.5 mab

Data Processing

Suspended sediment concentration was determined from the acoustic backscatter of the ADCPs, as detailed in the Appendix, and of the ADVs, as described by Brand et al. (2010).

Velocities and SSF are reported using along-channel x and cross-channel y components, with positive x in the

flood direction (SE) and positive y towards the shallows (NE) (Fig. 1). For each station, the along-channel direction was defined as the principal direction during ebb tides, to account for variations due to local bathymetry and to avoid the influence of potential compass errors. At the shallow (shoulder and flats) stations, the flood and ebb tide current directions were separated by significantly less than 180° , and the direction of ebb currents was much more narrowly focused than that of floods. At slope and channel stations, flood and ebb currents were opposite in direction, as expected. Tidally averaged quantities were calculated from time series by applying a low-pass Butterworth filter with stop-frequency of 0.025 h^{-1} and pass-frequency 0.033 h^{-1} .

The effect of suspended sediment on fluid density ρ_C was calculated as follows:

$$\rho_C = \text{SSC} + \rho_w(1 - \text{SSC}/\rho_s)$$

where SSC is mass concentration of sediment, water density $\rho_w = 1,020 \text{ g/L}$, and sediment density $\rho_s = 2,300 \text{ g/L}$. Significant wave heights, wave periods, and bottom orbital velocities were calculated from ADV velocity and pressure data following (Madsen 1994). Wind stress was calculated from wind speed W_s measured at San Francisco International Airport as $\tau_w = C_d \rho_{\text{air}} W_s^2$, using air density $\rho_{\text{air}} = 1.22 \text{ kg/m}^3$ and drag coefficient $C_d = 1.2 \times 10^{-3}$ (Pond and Pickard 1983).

Suspended Sediment Flux Decomposition

Tidally averaged SSF was calculated as follows:

$$\text{SSF} = \overline{\mathbf{u}hc} \quad (1)$$

where \mathbf{u} is along-channel (u) or cross-channel (v) velocity, h is depth, c is SSC, overbar denotes depth average, and angle brackets denote tidal average. At stations instrumented with ADCPs, in the region between the lowest measured value and the bed velocities were assumed to vary logarithmically, whereas SSC was assumed constant. The assumption of constant near-bed SSC results in a conservative estimate of near-bed SSC and SSF. At the shallow stations, the data from one or two elevations were assumed to represent a depth-averaged value, and the contribution to SSF of correlations between the vertical structures of \mathbf{u} and c was neglected.

The depth-averaged approach was compared to SSF calculated from Rouse profiles of SSC and logarithmic velocity profiles, and results indicate that the level of error introduced by neglect of vertical structure would not influence our conclusions. For a settling velocity of 2 mm/s and friction velocity u_* of $0.005\text{--}0.02 \text{ m/s}$, the ratio between the value at 0.50 mab and the depth average is $1.08\text{--}1.65$ for SSC and $1.3\text{--}1.67$ for SSF, with the lower SSF value

corresponding to more energetic conditions when transport is greater. At times when the velocity profile deviated significantly from logarithmic, the error may have been greater.

SSF was decomposed to investigate mechanisms responsible for transport, as follows. On the right-hand side of Eq. 1, depth is expressed as $h = \langle h \rangle + h_t$, where the subscript t denotes the residual from a tidal average. \mathbf{u} and c are expressed as the sum $x = \langle \bar{x} \rangle + \bar{x}_t + x'_z$ of depth and tidally averaged, tidal residual of the depth-averaged quantity, and a depth-dependent residual. As stated above, the depth-varying residual was not resolved at the shallow stations.

Multiplication of the three decomposed time series followed by tidal and depth averaging generates seven nonzero terms. Three of these terms were calculated for all stations. Advective (AD) flux $\langle \bar{\mathbf{u}} \rangle \langle h \rangle \langle \bar{c} \rangle$ accounts for transport by the depth-averaged mean flow, tidal cycle correlation (TCC) flux $\langle \bar{\mathbf{u}}_t \rangle \langle h \rangle \langle \bar{c}_t \rangle$ is the transport produced by the correlation of tidally varying velocity and SSC, and Stokes drift (SD) flux $\langle \bar{\mathbf{u}}_t h_t \rangle \langle \bar{c} \rangle$ is the transport produced by the correlation of tidally varying velocity and depth. Two additional terms, which account for the correlation of the vertically varying components of velocity and SSC, were computed for the ADCP stations. In this paper, the sum of these two terms is called depth correlation flux: $\text{DC} = \langle \bar{\mathbf{u}}'_z \rangle \langle h \rangle \langle \bar{c}'_z \rangle + \langle \bar{\mathbf{u}}'_z h_t \rangle \langle \bar{c}'_z \rangle$. The two remaining terms, $\langle \langle \bar{\mathbf{u}} \rangle h_t \bar{c}_t \rangle$ and $\langle \bar{\mathbf{u}}_t h_t \bar{c}_t \rangle$, are not discussed as they typically constitute a small fraction of total SSF and are not clearly linked to forcing mechanisms.

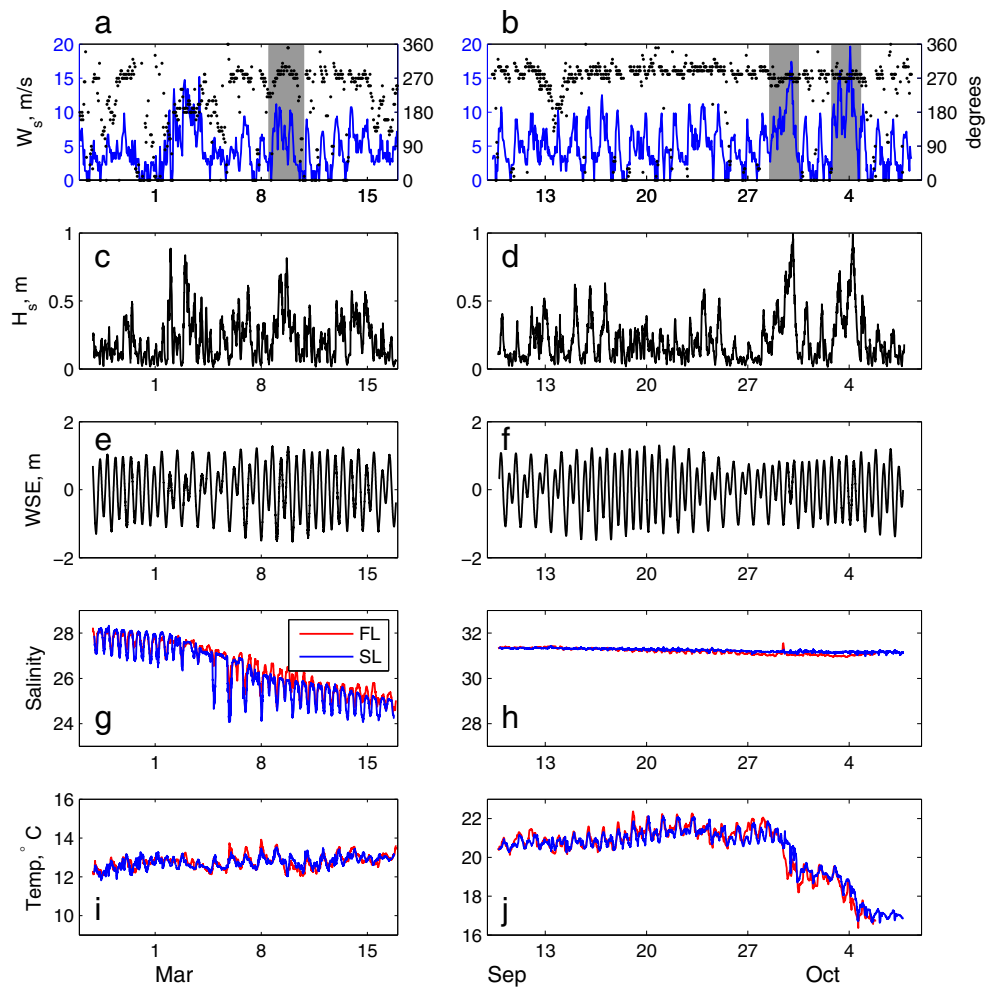
Results

Conditions During the Deployments

The winter of 2009 was relatively dry. At the beginning of the winter deployment, salinities (psu) in the study area were approximately 28, with tidal variation at the surface (an indicator of the longitudinal salinity gradient) of 1 at Slope Mid (Fig. 2g). A southerly storm on 2–4 Mar (Fig. 2a) produced significant freshwater inflows, and during 3–8 Mar salinities decreased and the longitudinal salinity gradient increased. During this period, salinities over the flats were slightly higher than near-surface salinities in the channel. There were sustained westerly winds on 8–10 Mar, and significant wave heights were greater than 0.3 m at Flats for 1.5 days (Fig. 2c). The wind-wave response to the southerly winds on 2–4 Mar was more erratic. Temperatures varied little during the winter deployment.

In the summer deployment, the daily westerly sea breeze generated short periods of wind waves $0.3\text{--}0.5 \text{ m}$ high (Fig. 2b, d). During 29–30 Sep and 3–4 Oct, westerly winds exceeding 15 m/s produced wave heights over 0.5 m (peak

Fig. 2 Meteorologic and oceanographic conditions during the winter (*left*) and summer (*right*) deployments. **a, b** Wind speed and direction measured at San Francisco International Airport, with wind events discussed in the text shaded. **c, d** Significant wave height at Flats (FL). **e, f** Water surface elevation, showing spring–neap tidal cycle. **g, h** Salinity at FL and Slope Mid (SL: near-surface in winter and near-bed in summer). **i, j** Temperature at FL and SL (near-surface in winter and near-bed in summer at SL)



1 m) that were sustained for more than a day. As an indication of the frequency of these conditions, hourly wind speed at San Francisco International Airport exceeds 11 m/s 0.5 % of the time in Oct, or an average of 3.7 h of the month, based on a 30-year record (www.wcc.nrcs.usda.gov/climate/windrose.html). In the events we observed, wind speed exceeded 11 m/s for more than 10 h. During the wind events, atmospheric temperatures dropped, leading to a decrease in water temperature of approximately 2 °C during each event (Fig. 2j). There was no precipitation during the deployment, and salinities were close to marine, with negligible spatial or temporal variation.

Bed Sediment Grain Size

Bed sediments throughout the study area were predominantly silt (Fig. 3). Spatial variation in grain size distribution was greater than temporal variation. The average fraction of sand and gravel was 0.016 in the channel, significantly less than the average of 0.07–0.14 at the other stations. Slope Mid had the greatest average fraction of sand and gravel and the lowest fraction of silt, indicating that grain size is

slightly coarser at the shoal–channel interface than in either the channel or shallows. Results from Slope Mid were more variable than the other stations, which may reflect greater temporal variability but is more likely due to the large uncertainty in depth associated with inaccuracy in sampling location in this region of steep slope.

Suspended Sediment Concentration and Flux

The magnitude and direction of SSF varied with cross-channel position due to variation in both tidal currents and SSC across the transect. The range of SSC was much greater at the shallow stations than in the channel, due to the strong dependence on wind-wave energy in the shallows (Fig. 4a, b). Maximum SSC at Flats during the two strong wind events at the end of the summer deployment was almost three times greater than at any other time during the deployments. SSC at all stations varied with the daily and spring–neap tidal cycles, but tides accounted for more of the variation at the slope and channel stations. Spring-tide SSC in the channel was greater during the summer than the winter deployment. Time series of cumulative

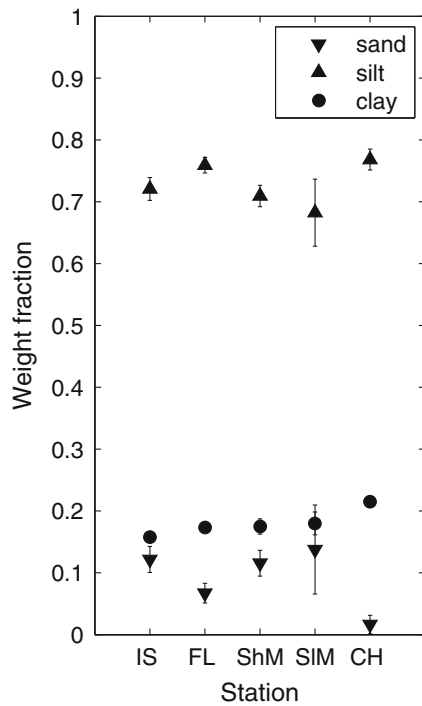


Fig. 3 Fractions (mean \pm standard deviation) of sand and gravel, silt, and clay in bed sediment samples from five stations (see Fig. 1 for locations). $N = 5$ for SL, $N = 6$ for all other stations

SSF show significant temporal variability, and differences in both magnitude and direction between the shallows and the channel (Fig. 4). The greatest rate of flux (steepest slope of cumulative transport) typically occurred at the times of greatest SSC. At the shallow stations, the majority of both the along-channel and cross-channel cumulative SSF for each deployment occurred over just a few days, during wind events with elevated wave energy and SSC lasting more than 24 h. Most transport from the shoal to the channel also occurred during these wind events. On the slope, cross-channel SSF was directed towards the channel during both winter and summer wind events. In the shallows, SSF_y during the March wind event was directed landward, whereas in the summer wind events, it was channelward (Fig. 5). In Fig. 5, SSF results are averaged by depth zone to elucidate cross-channel variations in transport. Although differences were observed between longitudinal positions within the depth zones, they were less than the differences between zones.

Summer Wind Events

The westerly winds during the summer wind events produced a predominately along-channel wind stress τ_{wx} (Fig. 6a). In response, near-bed $\langle u \rangle$ at the shallow stations

Fig. 4 Time series of SSC and cumulative SSF during the winter (left) and summer (right) deployments. **a, b** SSC at Flats (FL) and the slope (SL). **c, d** Cumulative along-channel SSF at FL, SL, and Channel (CH). **e, f** Cumulative cross-channel SSF at the same locations. SL data are from Slope Mid before 5 Mar in winter and from Slope North after 5 Mar and in summer. Shading indicates sustained wind events

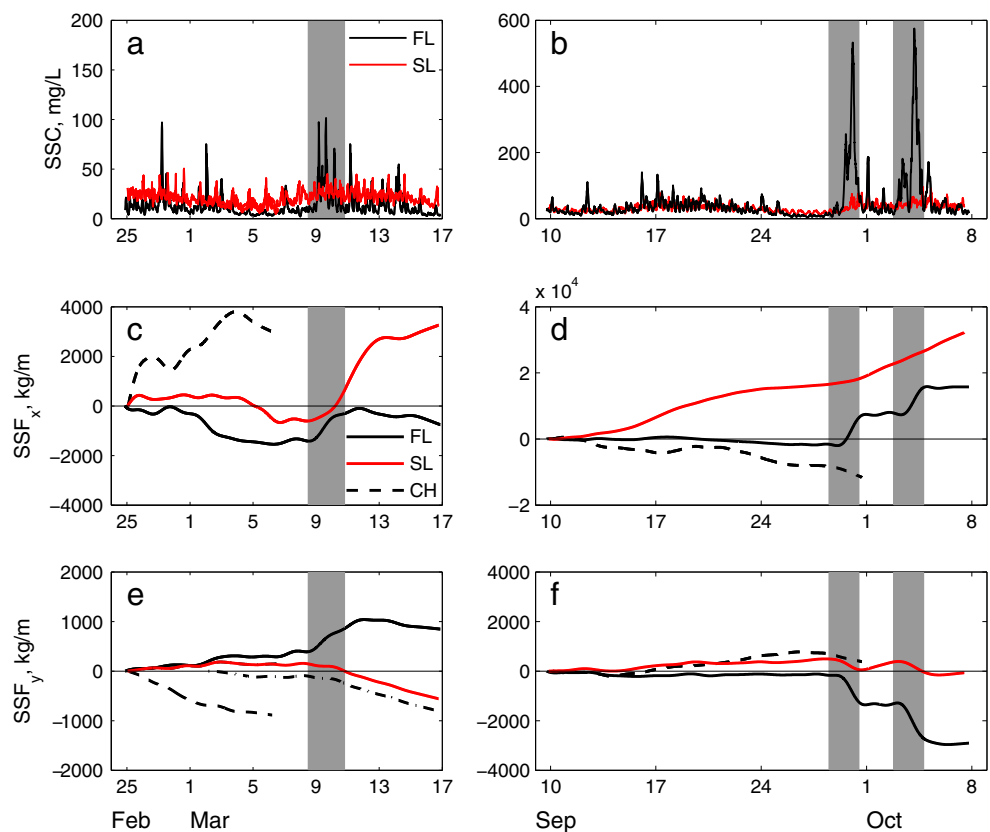
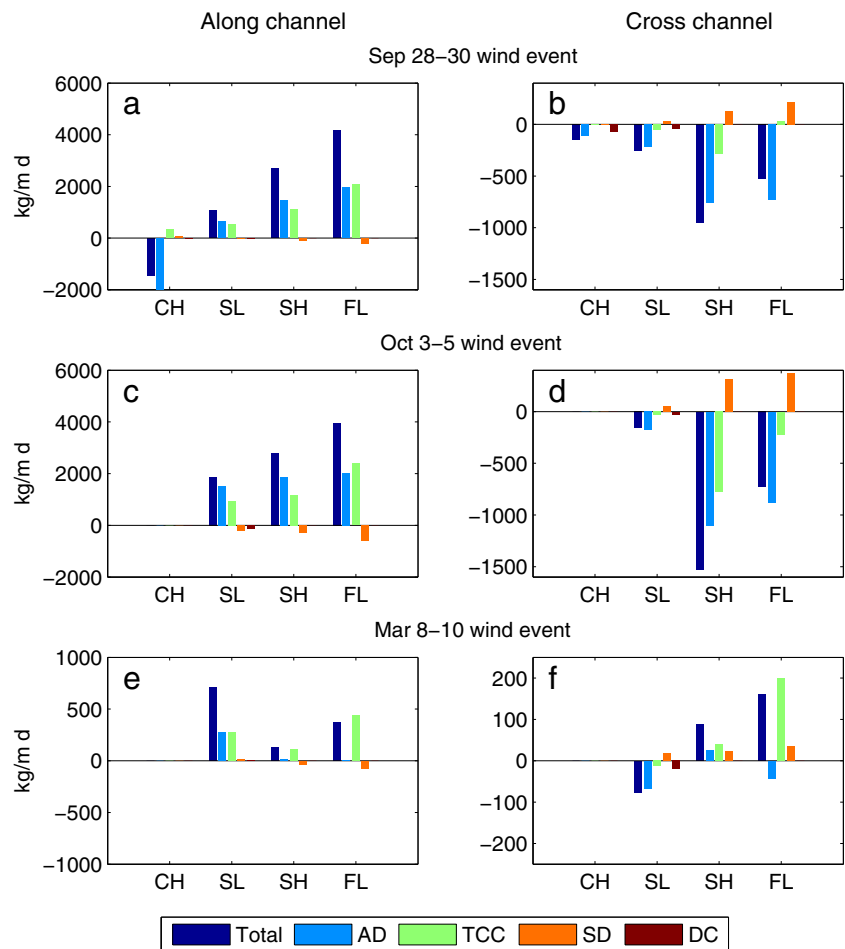


Fig. 5 Decomposed daily tidally averaged SSF in along-channel and cross-channel directions at the channel (*CH*), slope (*SL*), shoulder (*SH*), and flats (*FL*) for three sustained wind events: **a, b** 28–30 Sep; **c, d** 3–5 Oct; **e, f** 8–10 Mar. Components of SSF are advective (*AD*), tidal cycle correlation (*TCC*), Stokes drift (*SD*), and (for ADCP stations only) depth correlation (*DC*). Note the difference in y-axis scale between the upper two and lower subplots in both columns



was positive, whereas at the channel station ($\langle u \rangle$) was negative throughout the water column (Fig. 6b), consistent with observations by Walters (1982) that along-channel wind-driven circulation in South Bay is southeasterly over the shoals and slope and northwesterly in the channel. SSF_x followed the same spatial pattern (Fig. 5a, c). This type of transverse separation between the current generated by wind shear and the barotropic return flow is typical of basins with variable bathymetry, because the strength of the return flow only exceeds the downwind current in regions with greater-than-average depth (Csanady 1973; Wong 1994).

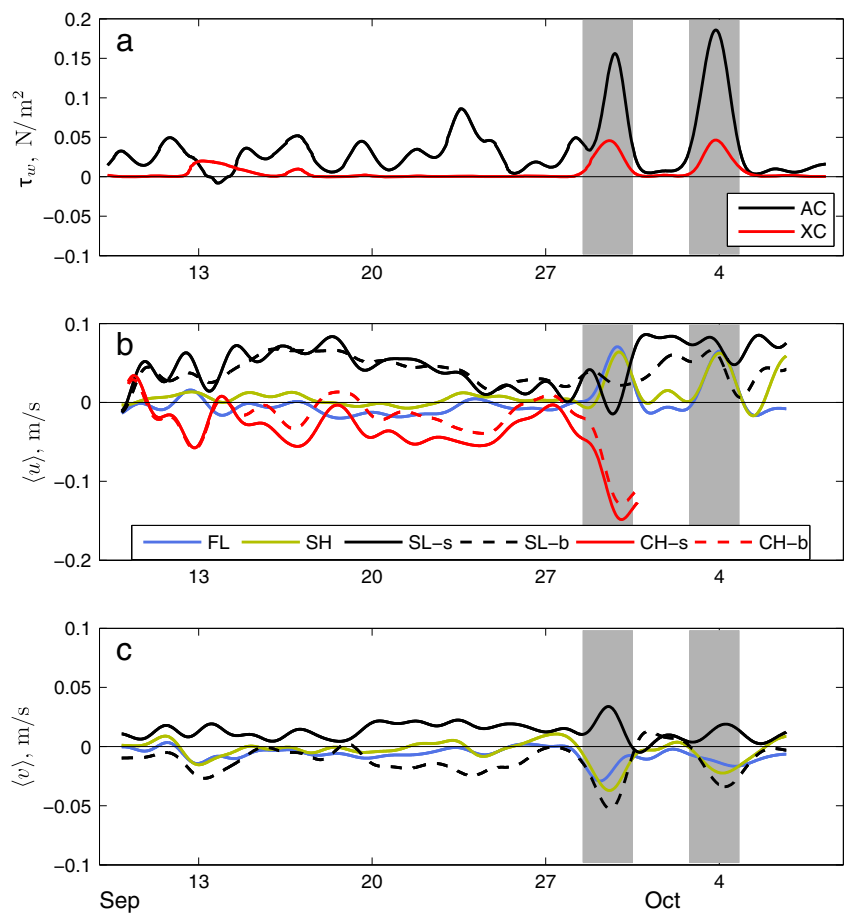
Cross-channel SSF during these events was negative throughout the transect and mostly advective (Fig. 5b, d). The negative SSF_y resulted from a combination of wind-driven and lateral baroclinic circulation. The cross-channel wind stress drove downwind flow near the surface and upwind return flow at depth across the uniform bathymetry of the shoals. The direction of the observed lateral circulation, negative near-bed ($\langle v \rangle$) on the flats and shoulder, and two-layer flow at the slope (Fig. 6c) was also consistent with the lateral baroclinic forcing during the wind events.

The baroclinic forcing was produced by lateral gradients of temperature and SSC. Atmospheric cooling during the wind events caused water temperatures to decrease more rapidly in the shallows than in the channel (Fig. 2j). During the first wind event, water temperature at Flats was at least 2 °C lower than at the surface on the slope for more than 24 h (Fig. 7b). Temperature at the shoulder oscillated between that of the flats and the slope, as the front between the warmer channel water and the cooler shallows water migrated back and forth across the shoulder region (Fig. 7b, 30 Sep). The lateral gradient in SSC was also high due to vigorous wind-wave resuspension in the shallows (Fig. 7a). At times, the SSC gradient accounted for as much as 20 % of the tidally averaged lateral density gradient $\langle d\rho/dy \rangle$ (Fig. 8a, b).

Momentum Balance

The relative importance of wind and baroclinic forcing to the lateral circulation can be assessed from the respective terms in the momentum equation. We assume a cross-channel momentum balance consisting of the barotropic

Fig. 6 **a** Along-channel (AC) and cross-channel (XC) wind stress. **b** Tidally averaged along-channel velocities at Flats (FL), Shoulder Mid (SH), Slope North 6.75 mab (SL-s) and 1.25 mab (SL-b), and Channel 13.5 mab (CH-s) and 2.5 mab (CH-b). **c** Tidally averaged cross-channel velocities at FL, SH, SL-s, and SL-b. Shading indicates sustained wind events



(wind-induced) and baroclinic pressure gradients and friction, neglecting acceleration, advection, and the Coriolis force:

$$-g \frac{\partial \eta}{\partial y} + \frac{g}{\rho_0} z \frac{\partial \rho}{\partial y} = \frac{\partial}{\partial z} \nu_t \frac{\partial v}{\partial z} \quad (2)$$

where g is gravitational acceleration, η is water surface elevation, ν_t is turbulent eddy viscosity, ρ_0 is mean density, ρ is deviation from mean density, and z is depth below the surface. In this formulation, vertical variation in the density gradient is neglected.

Fig. 7 Suspended sediment concentration and temperature 28 Sep–6 Oct. **a** SSC at Flats 0.35 mab (FL), Shoulder Mid 0.5 mab (SH), and Slope Mid 6 mab (SL). **b** Temperature at FL, Shoulder North 0.5 mab (SH), and Slope Mid 0.7 m below the surface (SL). Blue shading indicates flood tides ($u - \langle u \rangle > 0$ at SH)

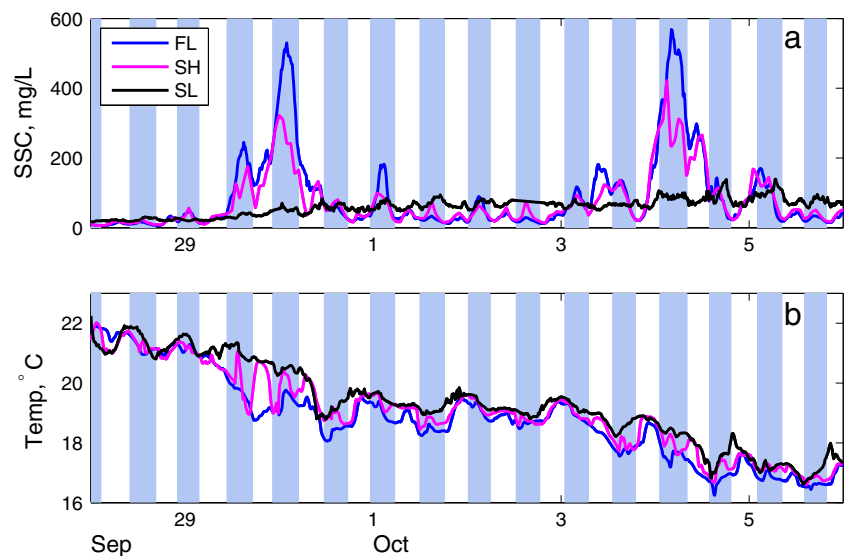
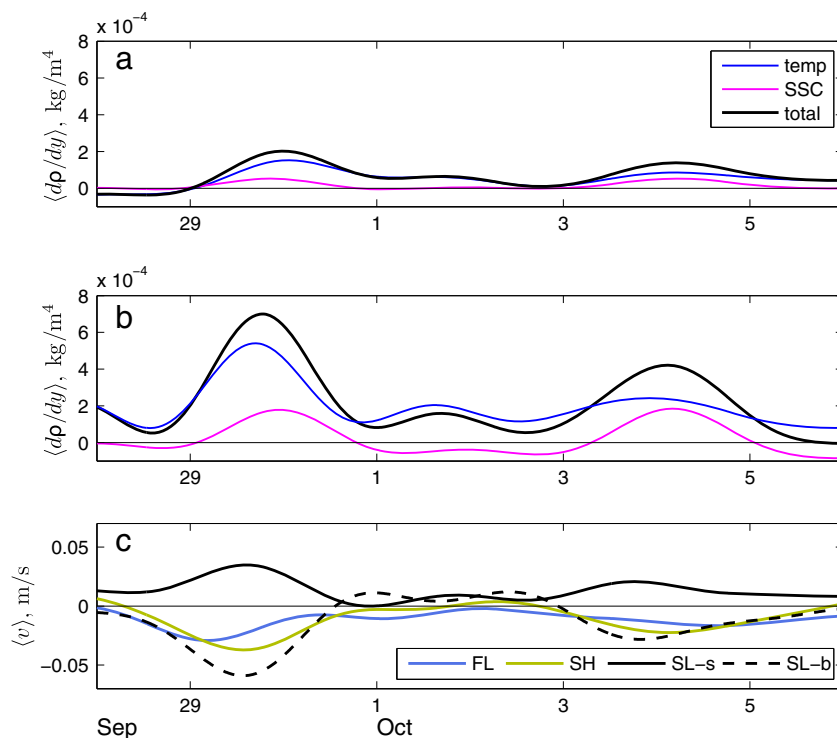


Fig. 8 Lateral density gradients and cross-channel velocities during the summer wind events. **a** Tidally averaged lateral density gradient ($\langle d\rho/dy \rangle$) between Flats (*FL*) and Shoulder Mid (*SH*), with contribution of SSC and temperature. **b** $\langle d\rho/dy \rangle$ between SH and Slope Mid (*SIM*), with contribution of SSC and temperature. **c** $\langle v \rangle$ 0.35 mab at *FL*, 0.25 mab at *SH*, and 1.8 mab (*SL-b*) and 7.3 mab (*SL-s*) at *SIM*



The barotropic pressure gradient due to wind shear scales as $g\tau_{wy}/\rho_0h$ and is independent of z . The baroclinic pressure gradient near the bed scales as $(gh/\rho_0)d\rho/dy$. The barotropic term is inversely related to depth, while the near-bed baroclinic term varies directly with depth, so the relative importance of the two terms varies across the study transect. In the shallows, for $\langle h \rangle = 3.8$ m, $\tau_{wy} = 0.05$ N/m², and $\langle \partial\rho/\partial y \rangle = 2.1 \times 10^{-4}$ kg/m² (the maximum observed value between Flats and the shoulder), the maximum tidally averaged cross-channel barotropic pressure gradient scales as 1.3×10^{-5} m/s², and the baroclinic pressure gradient is very similar: 1.0×10^{-5} m/s². On the slope, where $\langle h \rangle = 8$ m and maximum $\langle \partial\rho/\partial y \rangle = 7 \times 10^{-4}$ kg/m², the estimated barotropic pressure gradient is 0.6×10^{-5} m/s², while the baroclinic pressure gradient is an order of magnitude greater: 5.6×10^{-5} m/s².

The estimates for the baroclinic pressure gradient may be biased by the assumption that the lateral density gradient is constant over depth, but the data do not indicate the direction of the bias. A second and probably more significant source of bias is the use of measured lateral density gradients between stations to estimate local gradients. $\langle \partial\rho/\partial y \rangle$ between the shoulder and Flats is an overestimate for Flats and an underestimate for the shoulder, whereas the direction of bias due to use of $\langle \partial\rho/\partial y \rangle$ between the slope and the shoulder is not clear.

The scaling indicates that on the flats, far from the channel, the wind-induced barotropic pressure gradient was an important component of the forcing. Closer to the channel,

where depth and the lateral density gradient were greater, baroclinic forcing dominated cross-channel circulation and SSF_y .

Estimates of the near-bed velocity produced by wind and baroclinic forcing lead to the same conclusion. The magnitude of the downwind velocity can be scaled as follows:

$$v(z) = \frac{\tau_{wy}h}{\rho_0\nu_t} \left[\frac{3}{4} \left(\frac{z}{h} \right)^2 - \frac{z}{h} + \frac{1}{4} \right] \quad (3)$$

following Wong (1994). Equation 3 assumes a momentum balance between wind shear and barotropic return flow, a rectangular cross-section, and constant eddy viscosity over depth. It predicts a maximum downwind velocity at the surface and a maximum return flow at $z = 2h/3$ with magnitude $v(0)/3$. Depth and tidally averaged eddy viscosity was scaled as $\nu_t = \kappa \langle u_* \rangle \langle h \rangle / 6$ (where $\kappa = 0.41$ is the von Kármán constant), based on vertical integration of a parabolic ν_t profile, resulting in $\nu_t = 2.5 \times 10^{-3}$ m/s² for the shallows. Setting $\tau_{wy} = 0.05$ N/m² and $h = 3.8$ m yields $v(0) = 0.02$ m/s and a maximum return velocity $v = -0.007$ m/s in the shallows. This estimate does not account for the contribution of wave setup to the barotropic pressure gradient.

The influence of the baroclinic pressure gradient on the velocity distribution can be estimated by neglecting the barotropic term in Eq. 2 and integrating

$$v(z) \sim \frac{g}{\nu_t \rho_0} \frac{d\rho}{dy} \frac{z^3}{6} \quad (4)$$

For $v_t = 2.5 \times 10^{-3} \text{ m/s}^2$ and the maximum $\langle \partial\rho/\partial y \rangle$ between the shoulder and slope, Eq. 4 predicts $\langle v \rangle = -0.11 \text{ m/s}$ at $z = 6.2 \text{ m}$ below the surface (mbs), which is comparable to the observed difference between $\langle v_s \rangle$ and $\langle v_b \rangle$ at the slope (the subscripts s and b denote near surface and near bed, respectively) (Fig. 8c). At $z = 3.9 \text{ mbs}$, predicted $\langle v \rangle$ is -0.027 m/s , accounting for most of $\langle v_b \rangle$ at the shoulder (at stations where v_s was not measured, we assume $\langle v_s \rangle = 0$, neglecting return flow, for this comparison). The maximum $\langle \partial\rho/\partial y \rangle$ between the flats and the shoulder yields $\langle v \rangle = -0.006 \text{ m/s}$ at $z = 3.5 \text{ mbs}$, which is much less than $\langle v_b \rangle$ at Flats and very similar to the estimate for the barotropic return velocity. The estimate for baroclinically driven $\langle v_b \rangle$ at Flats is an upper limit, because $\langle d\rho/dy \rangle$ between the shoulder and Flats was likely considerably greater than the local lateral density gradient at Flats. The warmer channel water which intermittently affected temperatures on the shoulder did not reach Flats (Fig. 7), and lateral differences in SSC are unlikely due to the flat bathymetry. We conclude that far from the channel, the barotropic component of the pressure gradient from wind and wave setup exceeded the baroclinic component.

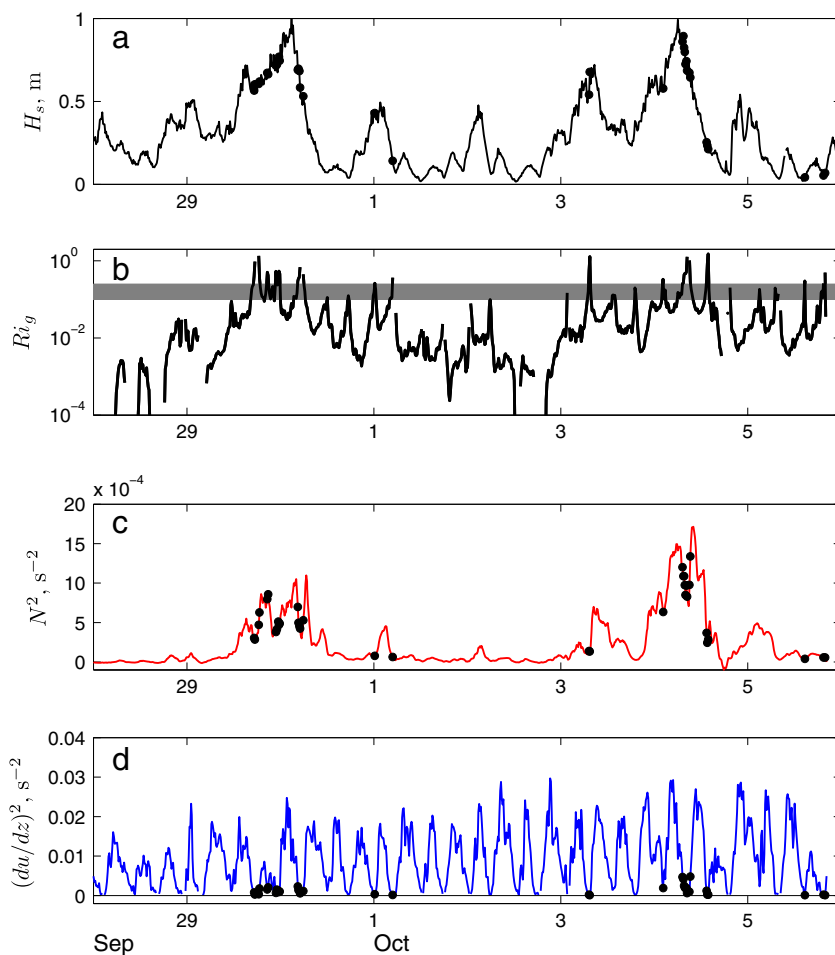
Density Stratification

During the wind events, turbulent mixing due to the combination of waves and tidal currents contributed to the high levels of SSC. However, at slack water, reduced mixing and sediment settling generated stable stratification, as indicated by the gradient Richardson number:

$$Ri_g = -\frac{g}{\rho_0} \frac{\partial\rho}{\partial z} \left(\frac{d\sqrt{u^2 + v^2}}{dz} \right)^{-2}$$

$Ri_g > 0.25$ indicates stable stratification. Ri_g calculated from three-point moving averages of current speed and SSC at 0.35 and 0.7 mab at Flats indicates that the water column was intermittently stably stratified due to the vertical gradient in SSC during the periods of elevated wave energy (Fig. 9) (vertical gradients in temperature were negligible). The stable stratification occurred around times of slack water, when u (but not necessarily v) was minimal. At these times, SSC and N^2 decreased, but less rapidly than the squared velocity shear. Stable stratification reduces vertical turbulent mixing, enhancing two-layer circulation, which, in

Fig. 9 Stable stratification at Flats during the summer wind events. **a** Significant wave height. **b** Gradient Richardson number (Ri_g), calculated from current speed and SSC 0.35 and 0.7 mab. *Gray stripe* indicates threshold between well-mixed (below) and stably stratified (above). **c** Buoyancy frequency (N) squared. **d** Shear in speed squared $\left(d\sqrt{u^2 + v^2}/dz \right)^2$. *Black dots* in **a**, **c**, and **d** indicate bursts for which $Ri_g > 0.25$



this case, contributed to the channelward near-bed SSF over the flats.

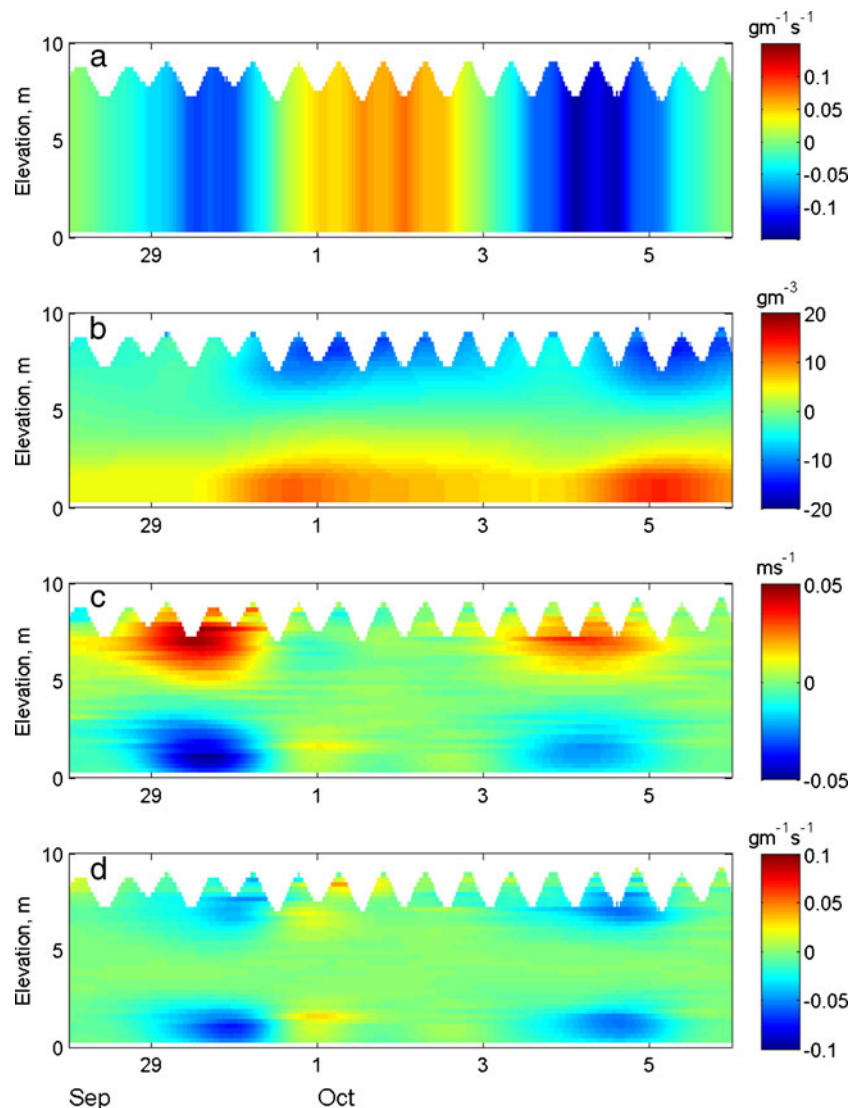
Influence on Decomposed SSF

When baroclinic circulation is directed along-channel, the sheared up-estuary flow is typically compensated by down-estuary barotropic flow, yielding a near-zero tidally and depth-averaged value and no associated advective SSF. However, for lateral baroclinic circulation, the compensating barotropic flow is not constrained to the cross-channel direction, and the depth-averaged residual may be nonzero, as occurred in this study. The negative near-bed $\langle v \rangle$ was greater than the positive $\langle v \rangle$ higher in the water column at the slope (Fig. 8c) and channel stations, resulting in negative $\langle \bar{v} \rangle$ and negative advective cross-channel SSF (Fig. 10a).

The lateral circulation also generated negative (although relatively small) depth correlation SSF_y on the slope, due to the correlation of greater-than-average SSC with negative $\langle v \rangle$ near the bed, and the opposite near the surface (Fig. 5b, d and Fig. 10b–d). At the shallow stations, the barotropically and baroclinically driven increase in negative near-bed $\langle v \rangle$ enhanced advective SSF_y. The assumption that near-bed SSC and velocity represent depth-averaged values at these stations overestimates SSF_y during the wind events.

While this analysis has focused on tidally averaged forcing, the lateral circulation and sediment exchange were not gradually varying, but intermittent. During the summer wind events, two-layer cross-channel pulses at the slope occurred primarily during ebb tides and were stronger ($v_s - v_b$ up to 0.3 m/s) and persisted longer than at any other time in the two deployments. The pulses generated two-layer SSF_y. The steep grade of the channel slope enhanced the

Fig. 10 Components of cross-channel SSF at Slope North as a function of depth, 28 Sep–5 Oct. **a** Advective SSF_y, distributed across depth $\langle \bar{v} \rangle \langle \bar{c} \rangle \Delta h$. **b** Tidal average of deviation from depth-averaged SSC $\langle c'_z \rangle$. **c** Tidal average of deviation from depth-averaged v $\langle v'_z \rangle$. **d** Tidally averaged depth correlation SSF_y $\langle c'_z \rangle \langle v'_z \rangle \Delta h$

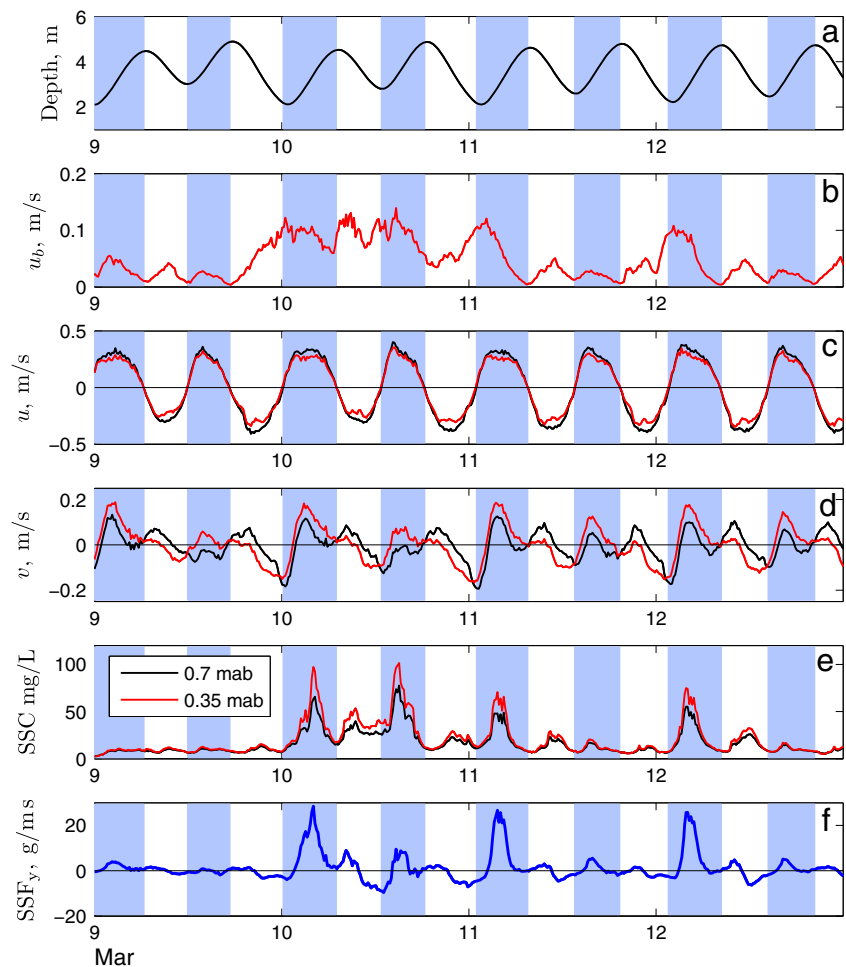


gravitational forcing of the baroclinically driven SSF which transported the sediment to the channel's edge.

Summary of SSF During the Summer Wind Events

Strong westerly winds elevated SSC through wind-wave resuspension and generated barotropic return flow towards the channel in the eastern shoals, driving negative SSF_y . At the same time, a temperature- and SSC-induced density gradient developed between the shallows and channel, which also generated negative near-bed $\langle v \rangle$ and SSF_y . In the shoulder region, both the barotropic and baroclinic components of the pressure gradients were important, because the lateral density gradient increased approaching the channel. Intermittent stable stratification in the shallows increased the potential for sheared cross-channel flows. At the channel slope, the negative near-bed SSF_y was dominated by baroclinic forcing, due to the greater depth and the strength of the density gradient.

Fig. 11 Time series from Flats during the Mar wind event, illustrating positive tidal cycle correlation SSF. **a** Depth. **b** Representative bottom orbital velocity. **c** Along-channel velocity. **d** Cross-channel velocity. **e** SSC. **f** Instantaneous cross-channel SSF (average of vc at the two measurement elevations times depth). Blue shading indicates flood tides ($u - \langle u \rangle > 0$)



Winter Wind Event

Wind speed and wave heights were lower during the Mar wind event than the summer events (Fig. 2) and were more typical of sustained wind events in South Bay. SSF was smaller in magnitude at all stations (Fig. 5). SSF at the shoulder and Flat stations was landward, dominated by a large positive tidal cycle correlation (TCC) term, due to greater SSC during flood than ebb tides on average (Fig. 11). The positive TCC SSF in the shallows was produced by increased wind-wave resuspension at low water, combined with vertical turbulent mixing during the following flood tides, as has been observed previously in South Bay (Brand et al. 2010; Lacy et al. 1996). τ_{wy} and the wind-induced barotropic pressure gradient were approximately three times lower than during the summer wind events and did not dominate the direction of SSF.

In contrast, SSF_y at the slope was channelward (Fig. 5f). The divergence in direction of SSF_y between the slope and shoulder was persistent following the 3–5 Mar freshwater inflows. As during the summer wind events, negative

advective SSF_y on the slope was produced by pulses of two-layer cross-channel velocities during ebb tides. The pulses of near-bed channelward current resulted from the development and subsequent breakdown of convergence fronts at the shoal–channel interface, driven primarily by the interaction of the lateral salinity gradient and turbulent mixing (Collignon and Stacey 2012). These pulses of lateral circulation occurred throughout the winter deployment, but the influence on tidally averaged exchange was greatest during the spring tides following the increase in lateral salinity gradient due to freshwater inflows. The Mar wind event fell during these spring tides, and the combination of elevated SSC and lateral baroclinic circulation produced the large negative SSF_y on the slope. Along-channel SSF at the slope was large and positive, with both positive advective and tidal cycle correlation components (Fig. 5e).

Typical Summer Conditions

The magnitude and spatial pattern of SSF were quite different during the typical summer seabreeze conditions of 9–27 Sep (Fig. 12). SSF_y at the slope was positive. In the

shallows, both cross- and along-channel SSF were minimal during both neap and spring tides, despite greater SSC than that during the winter deployment. In the cross-channel direction, negative advective SSF was mostly offset by positive Stokes drift SSF . While both the AD and SD components were greater during spring than neap tides due to increased SSC, the sum of the two was less.

The maximum along-channel SSF during this period occurred on the slope and was directed up-estuary (Fig. 12a, c). Tidal currents were stronger during floods than ebbs at the slope during the summer deployment (Fig. 13a). As a result, SSC peaked twice a day, toward the end of flood tides, whereas in the shallows peaks in SSC occurred during both flood and ebb tides (Fig. 13b, e). The up-estuary $\langle u \rangle$ generated positive advective SSF_x , and the greater SSC during floods than ebbs produced positive TCC SSF_x (Fig. 12a-d).

Influence of Freshwater Inflows

Freshwater inflows have the potential to influence the exchange of sediment between channel and shoals both by

Fig. 12 Decomposed daily tidally averaged SSF in along-channel and cross-channel directions at the channel (CH), slope (SL), shoulder (SH), and flats (FL) for a, b well-mixed neap tides (11–14, 25–27 Sep); c, d well-mixed spring tides (17–22 Sep); e, f a calm, weakly stratified period (12–16 Mar). Components of SSF are advective (AD), tidal cycle correlation (TCC), Stokes drift (SD), and (for ADCP stations only) depth correlation (DC)

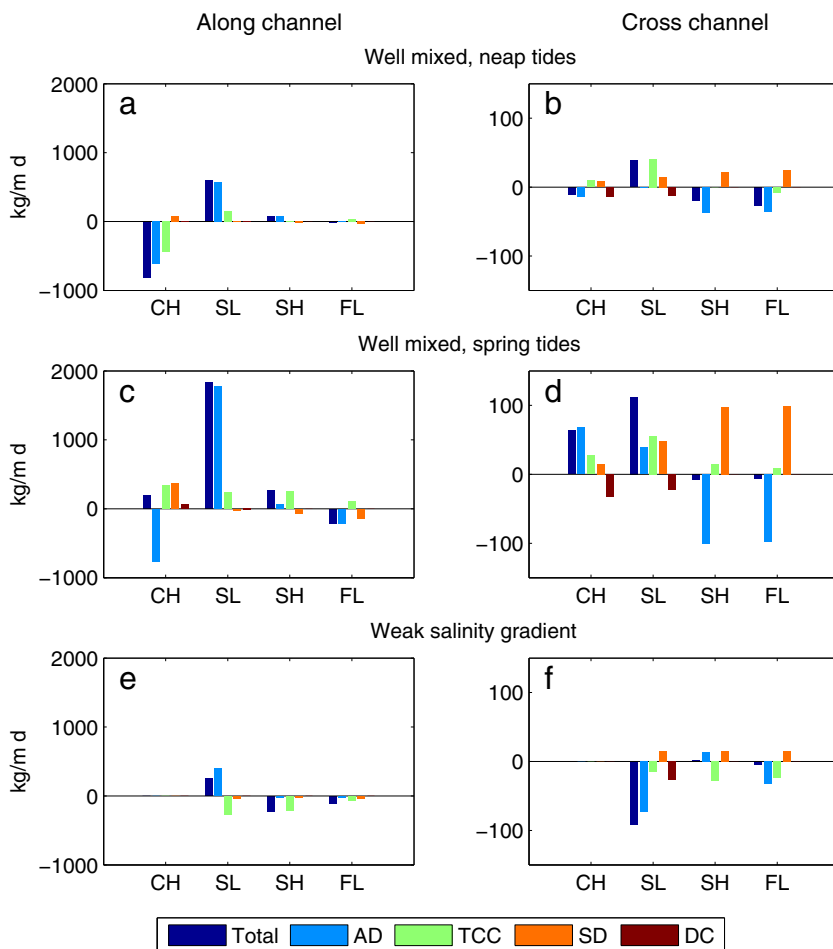
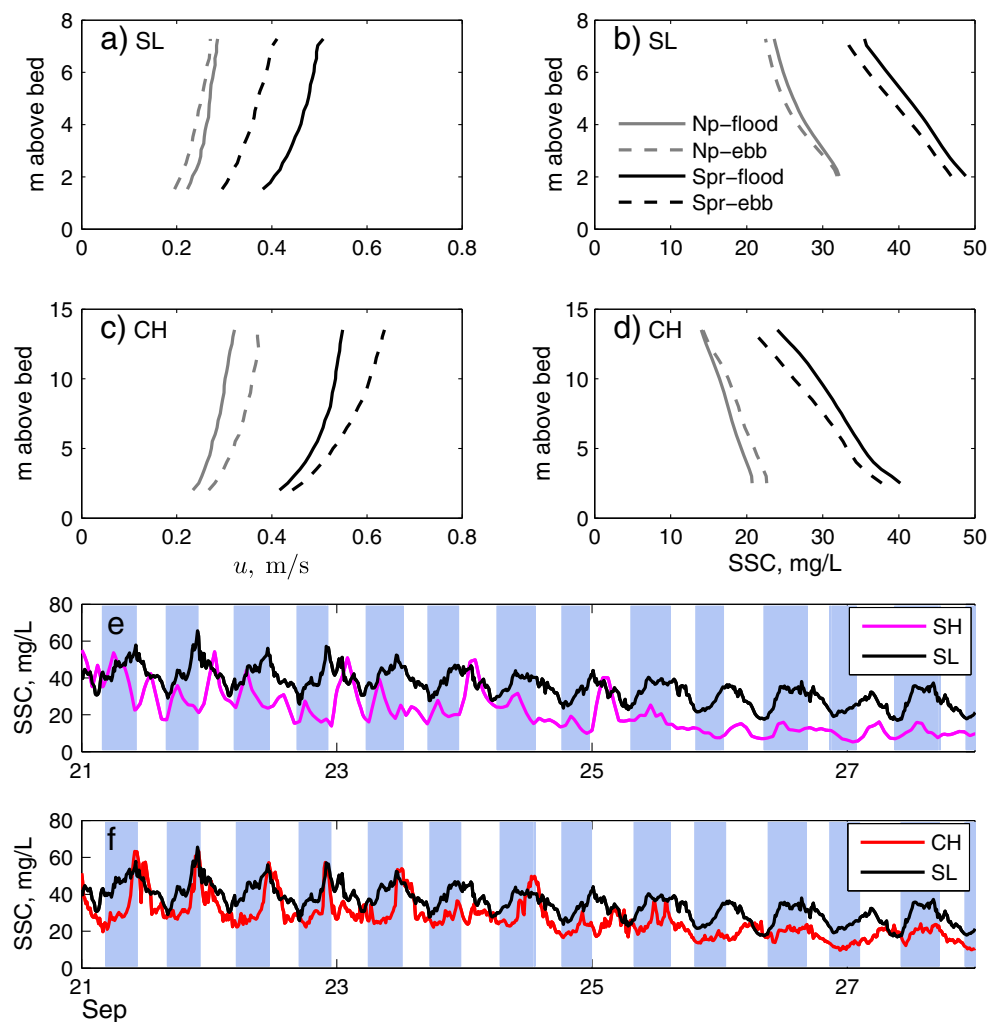


Fig. 13 Phase-averaged profiles of along-channel velocity at **a** Slope Mid (*SL*) and **c** Channel (*CH*); and SSC at **b** *SL* and **d** *CH*, for flood and ebb tides, during spring and neap tides in summer deployment. **e** SSC at Shoulder Mid, 0.25 mab (*SH*); and *SL* 2 mab. **f** SSC at *CH*, 2 mab; and *SL*, 2 mab. Blue shading indicates flood tides ($u - \langle u \rangle > 0$ at *SH*)



distributing river-borne sediment (shoalward) and by generating lateral baroclinic transport (channelward or shoalward). The freshwater inflows of 3–8 Mar produced the second of these effects, but not the first. SSC was low during the event, suggesting that any newly introduced riverine sediment did not reach the study area (Fig. 2k). Following the freshwater inflows, a lateral salinity gradient developed and persisted until the end of the deployment (16 Mar). The lateral salinity gradient drove baroclinic circulation and negative SSF_y at the slope which continued during 12–16 Mar (Fig. 12f).

Along-channel SSF was also influenced by the increase in longitudinal salinity gradient ds/dx caused by the freshwater inflows. SSF_x during 12–16 Mar was up-estuary in the channel and down-estuary in the shallows, whereas during the summer, when ds/dx was negligible, the opposite spatial pattern occurred (Fig. 12a, c, e). Similar influence of the longitudinal salinity gradient on SSF has been observed in other estuaries and has been attributed to either baroclinic circulation or tidal cycle correlation flux due to reduced stratification and enhanced vertical mixing during

flood compared to ebb tides (Scully and Friedrichs 2007; Sommerfield and Wong 2011; Ralston et al. 2012).

Discussion

Importance of Lateral Baroclinic Forcing to Shoal–Channel Exchange

Our results indicate that lateral baroclinic forcing was critical to transport of suspended sediment from shallows to channel. At all times when tidally averaged cross-channel SSF was negative at the slope, it was dominated by baroclinically driven flux. During the winter deployment, SSF_y at the slope was negative following the increase in lateral salinity gradient produced by the freshwater inflows of 2–4 Mar. Cross-channel circulation, as indicated by the shear in $\langle v \rangle$ at the slope, increased at this time. During the summer wind events, barotropic return flow produced negative SSF_y far from the channel, but the channelward SSF_y at

the slope was driven by lateral gradients in temperature and SSC. The tidally averaged lateral density gradients during the summer wind events were comparable in magnitude to that of the winter deployment. Between the shoulder and the slope, $\langle \partial\rho/\partial y \rangle$ reached a maximum of 9.7 kg/m^4 during the freshwater inflows. During 7–15 Mar, $\langle \partial\rho/\partial y \rangle$ averaged 6.5 kg/m^4 , and the top-to-bottom difference in $\langle v \rangle$ at Slope Mid was 0.08 m/s , very similar to conditions during 28–30 Sep (Fig. 8). Although water exchange between the shallows and channel was greater during the winter than summer, because of the longer duration of the lateral density gradient, sediment exchange was much greater during the summer wind events, due to the greater SSC.

In winter, the lateral density gradient was generated by differential advection of a longitudinal salinity gradient. A longitudinal density gradient contributes to up-estuary SSF_x in the channel, either through gravitational circulation or due to tidal straining (Simpson et al. 1990). Thus, the freshwater inflows increased both the negative cross-channel SSF and the positive along-channel SSF at the slope, and up-estuary transport in the channel served to retain sediment in the estuary. The lateral gradients of temperature and SSC during the summer wind events were not associated with a longitudinal density gradient, so SSF_y and SSF_x were not coupled in the same manner. Along-channel SSF was negative in the channel during the summer wind events, enhanced by down-estuary wind-driven return flow.

Broader Implications

Data quantifying SSF across a transect from the shallows to the channel in San Francisco Bay were not available before this study. In this section, we evaluate the broader spatial and temporal implications of our results to shoal–channel exchange of sediment as well as other particles and dissolved substances in South Bay. While this data set captured a variety of forcing conditions, it is limited in sampling only a fraction of the annual cycle. Long-term measurements at the Dumbarton Bridge show that SSF and the sediment budget in South Bay vary not only seasonally, but from year to year (Shellenbarger et al. 2013).

Krone (1979) postulated that sediments are supplied to the shoals of San Francisco Bay during freshwater inflow events and gradually winnowed off the shoals during the summer sea breeze season, which is consistent with the paradigm of concentration gradient driven transport described by Friedrichs (2011). Our observations show that during sea breeze conditions, SSC in the shallows is elevated, but SSF is minimal. Cross-channel SSF in the shallows was negative and small in magnitude, while SSF_y at the slope was positive and much greater. Thus, processes associated with the spatial SSC gradient did not dominate

transport, at least at the resolved temporal scales. Turbulent lateral shear dispersion, which is not resolved by the burst-averaged measurements reported here, undoubtedly produced some channelward flux at the shoal–channel interface, but the magnitude of this flux is estimated to be small, because the region of strong gradients in SSC between the channel and flats is narrow.

Sustained wind events were more effective at moving sediment off the shoals. In the moderate Mar wind event, SSF_y at the slope was negative due to lateral baroclinic forcing, while cross-channel SSF over the shoals was positive. During the extreme late-summer wind events, the export of sediment to the channel was much greater. The negative SSF_y was driven over the shoals by barotropic wind return flows, and across the shoulder and slope by lateral baroclinic forcing. These results suggest that, while wind-wave resuspension is a necessary component of elevated SSF, most channelward transport occurs in large episodic pulses rather than through gradual winnowing. Both sustained strong winds and falling temperatures were required to produce the large late-summer shoal-to-channel transport. Wind events of this intensity occur less than once a year (on average), but the magnitude of SSF during the events we observed suggests that such events may comprise a significant fraction of decadal-scale shoal–channel exchange.

Schoellhamer (1996) observed pulses of increased SSC from the shallows reaching the channel in South Bay at the end of large ebb tides and attributed them to greater cross-channel tidal excursion during spring tides. In our observations, channelward SSC pulses were primarily baroclinically driven. They were most likely to occur during large ebbs, but, even during spring tides, the cross-channel tidal excursion was not great enough to transport sediment to the channel unless it was enhanced by baroclinic forcing. In summer, peaks in SSC at the shoulder during spring-tide ebbs did not reach the slope or channel (Fig. 13e, f), but in winter, they did. After the winter freshwater inflows, the greater tidal excursion during spring tides enhanced differential advection, strengthening the lateral baroclinic gradient and the subsequent lateral pulses. We conclude that large ebbs only advect suspended sediment from the shallows to the channel at times when the South Bay is influenced by freshwater inflows or another source of lateral baroclinic forcing. This result depends on the bathymetry of our study site, specifically extensive, longitudinally homogeneous shoals, which characterizes much of South Bay. Tidal advection would play a stronger role in more complex bathymetric settings, such as the Dumbarton Narrows, where the decreasing width of the shoals diverts along-channel transport into the channel, or in shallow subembayments connected to the main channel by narrow passages.

The lateral salinity gradient observed in this study was fresher in the channel than the shallows. The reverse lateral salinity gradient also occurs in South Bay, during periods of increasing salinity (Powell et al. 1989; Huzzey et al. 1990; Gross et al. 1999). With the shoals fresher than the channel, baroclinically driven lateral exchange would be less effective at transporting sediment into the channel, as SSC is lower in the upper water column. In addition, the plunging at the channel slope which enhanced channelward transport in our observations would not occur.

The importance of baroclinically driven lateral advective transport to total SSF in this study suggests that the same mechanism may be critical to the exchange between shallows and the channel of other types of particles, such as phytoplankton, and dissolved substances, such as nutrients. Most phytoplankton blooms occur in spring, when lateral salinity gradients are likely. Thompson et al. (2008) documented phytoplankton dynamics in South Bay for 5 years and showed that blooms typically start on the eastern shoals and expand and migrate towards the channel. They observed one phytoplankton bloom that occurred in fall, exhibited little growth, and did not reach the channel. The seasonal absence of a lateral density gradient may have contributed to the lack of development of the fall bloom.

Conclusions

In estuaries, the influence of salinity on density typically far outweighs that of temperature or SSC. In South San Francisco Bay, where freshwater inflows are seasonal, density effects are generally considered negligible in the dry season. This study shows that lateral gradients in temperature and SSC can generate a baroclinic pressure gradient in South Bay comparable in strength to that generated by freshwater inflows, although with shorter duration. In a pair of late-summer wind events, a combination of lateral barotropic return flow and baroclinic forcing produced a massive transport of sediment from the shallows to the channel. Wind return flow was more important over the shallower landward portion of the shoals, and baroclinic forcing dominated near the shoulder and slope of the channel. At slack water during the strong wind events, the vertical gradient in SSC was strong enough to inhibit turbulent vertical mixing.

In South San Francisco Bay, lateral baroclinic forcing is critical to transporting suspended sediment from the shallows to the channel. At all times when tidally averaged cross-channel SSF at the channel slope was negative, it was dominated by baroclinic transport. In the absence of a lateral density gradient, tidally averaged SSF at the channel slope was positive. This suggests that sediment supply from

the shallows to the channel is limited during most of the summer sea breeze season.

Sustained winds increase SSF by an order of magnitude on the subtidal flats, compared to calm or sea breeze conditions. Along-channel SSF was up-estuary in the flats during wind events. Cross-channel SSF was negative during the strongest wind events, as described above, but was positive during a moderate wind event, primarily due to positive tidal cycle correlation flux. During calm or sea breeze conditions, SSF on the flats was an order of magnitude less than in the channel or on the slope.

Our observations from South San Francisco Bay highlight the distinctions between sediment dynamics in estuarine channels and shoals. These distinctions should inform the design and calibration of numerical models of estuarine sediment transport. In South Bay, resuspension is driven by tidal currents in the channel and predominately by wind waves in the shallows. The mechanisms governing transport also vary between the two environments. As a result, the magnitude, direction, and temporal variation in SSF can differ. Sediment transport at the interface between the shallows and channel is particularly complex, as it is influenced by sediment concentrations in both environments, as well as the frontal dynamics generated by the bathymetric transition.

Acknowledgments This work was supported by the National Science Foundation (OCE-0751970) and the Coastal and Marine Geology Program of the US Geological Survey. Thanks to Joanne Ferreira, Tim Elfers, Pete Dal Ferro, Jamie Grover, Rusty Holleman, Lissa MacVean, and Jim Christmann for assistance with field work, and to Dan Hoover for assistance in the laboratory. Theresa Fregoso prepared Fig. 1, and Angela Lam analyzed the bed sediment samples. Any use of trade, product, or firm names in this paper is for descriptive purposes only and does not imply endorsement by the US Government.

Appendix

Calculating SSC from ADCP backscatter involves two steps. First, relative backscatter S_v is determined from measured backscatter EI (echo intensity), to account for losses during signal transmission. Then, independent measurements of SSC and colocated values of S_v are used to solve for the calibration coefficients a and b of the log-linear relationship (Gartner 2004; Wall et al. 2006):

$$\log_{10} \text{SSC} = aS_v + b \quad (5)$$

The active sonar equation (Urlick 1967) describes an acoustic signal as it is transmitted through water, scattered by particles in the water, and measured by the instrument upon its return. The form of the equation used in this study is a combination of the equations used by previous

authors (Gartner 2004; Hoitink and Hoekstra 2005; Kim and Voulgaris 2003; Wall et al. 2006; Deines 1999):

$$S_v = 10 \log_{10} \left(\frac{1}{n} \sum_{i=1}^n 10^{(EI(i) - Er(i))K_c/10} \right) + 20\psi \log_{10} R + 2\alpha R + 2\alpha_s R \quad (6)$$

where Er is the echo intensity reference level; K_c is the conversion factor between counts (the unit of EI and Er) and dB; R is range, the along-beam distance from the transducer to the measurement location; α is water attenuation, a function of salinity, temperature, pressure, and acoustic frequency; and α_s is the sediment attenuation factor, a function of suspended sediment properties including concentration, particle radius and density, acoustic frequency, and water properties including kinematic viscosity, temperature, salinity, and pressure.

Equation 6 is solved for each vertical bin throughout the water column. The first term on the right-hand side is the measured signal strength, averaged across the n ADCP transducers, corrected for reference backscatter, and converted to dB. The second term is a correction for beam spreading. In this study, S_v was not corrected for transmit power, transmit length, or beam normalization due to lack of data. Wall et al. (2006) estimated the errors associated with omitting these corrections to be 5.1, 0.3, and 6.5 %, respectively.

For this calibration, ADCP frequency f ; fluid density ρ ; fluid viscosity ν ; R ; and the constants in calculating α were assumed to be known exactly. K_c was provided by the ADCP manufacturer. The EI data for Eq. 6 were averaged over 50 s (from 1-Hz data) and across the four transducers. The background intensity Er for each transducer was taken as the minimum value measured during each deployment (Gartner 2004). Salinity and temperature time-series data were taken from the instrument nearest the ADCP (Table 2).

Table 3 Results of ADCP calibrations to SSC

Deployment	Station	a	b	R^2	N
Winter	CH	0.026	-0.508	0.55	2,221
Winter	SIM	0.033	-0.955	0.71	3,642
Winter	SIN	0.029	-0.021	0.42	139
Summer	CH	0.025	-0.43	0.67	9
Summer	SIM	0.026	-0.119	0.70	2,706
Summer	SIN	0.027	-0.374	0.57	896
Summer	SIS	0.035	-0.647	0.70	3,381

a and b are the slope and intercept of the regression line, R^2 is the coefficient of determination, and N is the number of data points used in the calibration. Calibration data were time-series data from OBS for all stations except Channel in summer, which relied on SSC measured in grab samples

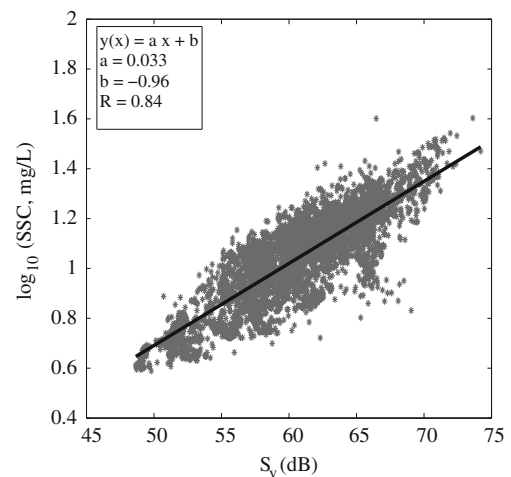


Fig. 14 SSC measured by OBS vs. corrected backscatter S_v from ADCP at Slope Mid, winter deployment, with regression results

Constant values for depth and pressure were used in calculating the speed of sound and α_s , because the tidal variations of these parameters have negligible effect. Mean and standard deviation of particle size were calculated from 5 days of data collected by the LISST deployed at Flats during each deployment (Brand et al. 2010). Although particle properties at Flats likely differed from those at the ADCP locations because of differences in water depth and velocities, these were the only available in situ measurements of particle size and were judged more representative than disaggregated bed sediment particle size. Aggregate density ρ_a was assumed to be $1,200 \text{ kg/m}^3$, similar to values reported for San Francisco Bay by Kranck and Milligan (1992).

The OBS sensors near the ADCPs were calibrated against SSC measured in field samples. Equation 5 was solved for a and b , using SSC measured by OBS and S_v , for each station and each deployment (Table 3, Fig. 14). Portions of the

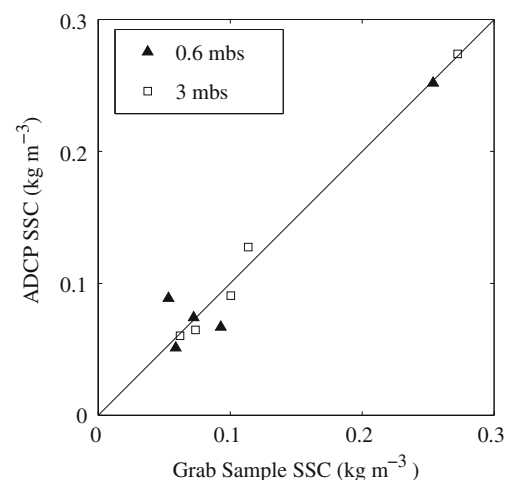
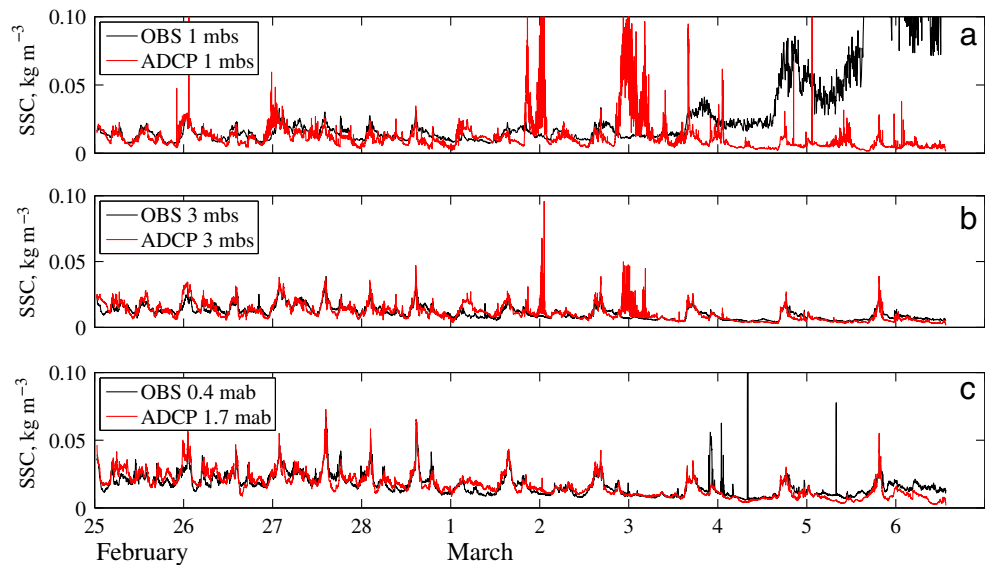


Fig. 15 SSC measured by the ADCP vs. SSC from grab samples at two depths at Slope Mid, winter deployment

Fig. 16 SSC measured by the ADCP and OBS at Slope Mid, winter deployment. **a** 1 m below surface (mbs). **b** 3 mbs (OBS data used in calibration). **c** Near bed: 1.7 m above bottom (mab) for ADCP, 0.4 mab for OBS



OBS data impacted by biofouling were not used in the calibrations, which, in some cases, was quite limiting. For the Channel station during the fall deployment, the field samples analyzed for SSC were used in Eq. 5, due to loss of the near-surface OBS. Comparison between SSC determined from the water samples and from ADCP backscatter at other stations generally showed good agreement (Fig. 15).

Time series of calibrated SSC measured at Slope Mid during the winter deployment are shown in Fig. 16. The calibration used the OBS located 3 m below the water surface (mbs). Comparison of SSC measured by the ADCP and the OBS 1 mbs reveals biofouling beginning 3 Mar. The elevated acoustic backscatter on 2 and 3 Mar, a period of high wind speed and wave height, is due to air bubbles entrained in the water column by surface waves. Time periods when air bubbles contributed to acoustic backscatter (identified by signal increasing with elevation) were excluded from the calibration time series.

References

- Brand, A., J.R. Lacy, K. Hsu, D. Hoover, S. Gladding, and M.T. Stacey. 2010. Wind-enhanced resuspension in the shallow waters of South San Francisco Bay: mechanisms and potential implications for cohesive sediment transport. *Journal of Geophysical Research* 115(11024). doi:10.1029/2010JC006172.
- Cheng, R., and J. Gartner. 1985. Harmonic analysis of tides and tidal currents in South San Francisco Bay, California. *Estuarine, Coastal, and Shelf Science* 21: 57–74.
- Collignon, A.G., and M.T. Stacey. 2012. Intratidal dynamics of fronts and lateral circulation at the shoal–channel interface in a partially stratified estuary. *Journal of Physical Oceanography* 42(5): 869–883. doi:10.1175/JPO-D-11-065.1.
- Conomos, T.J., R.E. Smith, and J.W. Gartner. 1985. Environmental setting of San Francisco Bay. In *Temporal dynamics of an estuary: San Francisco Bay*, chap. 1, eds. J.E. Cloern and F.H. Nichols, 1–12. Dordrecht: W. Junk Publishers.
- Csanady, G.T. 1973. Wind-induced barotropic motions in long lakes. *Journal of Physical Oceanography* 3(4): 429–438.
- Deines, K.L. 1999. Backscatter estimation using broadband acoustic Doppler current profilers. In *Proceeding of the IEEE 6th working conference on current measurements*. 249–253. San Diego.
- Friedrichs, C.T. 2011. Tidal flat morphodynamics: a synthesis. In *Treatise on estuarine and coastal science*, vol. 3, chap. 6, eds. J. Hansom and B. Flemming, 137–170. Amsterdam: Elsevier.
- Fugate, D.C., C.T. Friedrichs, and L.P. Sanford. 2007. Lateral dynamics and associated transport of sediment in the upper reaches of a partially mixed estuary, Chesapeake Bay, USA. *Continental Shelf Research* 27(11): 679–698. doi:10.1016/j.csr.2006.11.012.
- Gartner, J.W. 2004. Estimating suspended solids concentrations from backscatter intensity measured by acoustic Doppler current profiler in San Francisco Bay, California. *Marine Geology* 211: 169–187. doi:10.1016/j.margeo.2004.07.001.
- Gross, E.S., J.R. Koseff, and S.G. Monismith. 1999. Three-dimensional salinity simulations of South San Francisco Bay. *Journal of Hydraulic Engineering* 125: 1199–1209.
- Hoitink, A.J.F., and P. Hoekstra. 2005. Observations of suspended sediment from ADCP and OBS measurements in a mud-dominated environment. *Coastal Engineering* 52: 103–118. doi:10.1016/coastaleng.2004.09.005.
- Huzzey, L.M., J.E. Cloern, and T.M. Powell. 1990. Episodic changes in lateral transport and phytoplankton distribution in South San Francisco Bay. *Limnology and Oceanography* 35(2): 472–478.
- Kim, Y.H., and G. Voulgaris. 2003. Estimation of suspended sediment concentration in estuarine environments using acoustic backscatter from an ADCP. In *Proceedings of the international conference on coastal sediments 2003*. Clearwater.
- Kranck, K., and T.G. Milligan. 1992. Characteristics of suspended particles at an 11-hour anchor station in San Francisco Bay. *Journal of Geophysical Research* 97(C7): 11,373–11,382.
- Krone, R.B. 1979. Sedimentation in the San Francisco Bay system. In *San Francisco Bay: the urbanized estuary*, ed. T.J. Conomos, 85–96. San Francisco: Pacific Division of the American Association for the Advancement of Science.

- Lacy, J.R., D.H. Schoellhamer, and J.R. Burau. 1996. Suspended-solids flux at a shallow-water site in South San Francisco Bay, California. In *Proceedings, North American water and environment congress, June 23–28, 1996*, ed. C.T. Bathala. New York: American Society of Civil Engineers.
- Lacy, J.R., M.T. Stacey, J.R. Burau, and S.G. Monismith. 2003. The interaction of lateral baroclinic forcing and turbulence in an estuary. *Journal of Geophysical Research* 108(C3). doi:[10.1029/2002JC001392](https://doi.org/10.1029/2002JC001392).
- Lerczak, J.A., and W.R. Geyer. 2004. Modeling the lateral circulation in straight, stratified estuaries. *Journal of Physical Oceanography* 34(6): 1410–1428.
- Lucas, L.V., J.R. Koseff, S.G. Monismith, and J.K. Thompson. 2009. Shallow water processes govern system-wide phytoplankton dynamics: a modeling study. *Journal of Marine Systems* 75: 70–86. doi:[10.1016/j.marsys.2008.07.011](https://doi.org/10.1016/j.marsys.2008.07.011).
- Madsen, O.S. 1994. Spectral wave-current bottom boundary layer flows. In *In Proceedings of the 24th international conference on coastal engineering*, 384–398. ASCE.
- Pond, S., and G.L. Pickard. 1983. *Introductory dynamical oceanography*. Oxford: Butterworth-Heinemann Ltd.
- Powell, T.M., J.E. Cloern, and L.M. Huzzey. 1989. Spatial and temporal variability in South San Francisco Bay (USA). I. Distributions of salinity, suspended sediments, and phytoplankton biomass and productivity. *Estuarine, Coastal, and Shelf Science* 28: 583–597.
- Ralston, D.K., W.R. Geyer, and J.C. Warner. 2012. Bathymetric controls on sediment transport in the Hudson River estuary: lateral asymmetry and frontal trapping. *Journal of Geophysical Research* 117(C10013). doi:[10.1029/2012JC008124](https://doi.org/10.1029/2012JC008124).
- Schoellhamer, D.H. 1996. Factors affecting suspended-solids concentrations in South San Francisco Bay, California. *Journal of Geophysical Research* 101(C5): 12087–12095.
- Scully, M.E., and C.T. Friedrichs. 2007. Sediment pumping by tidal asymmetry in a partially mixed estuary. *Journal of Geophysical Research* 112(C07028). doi:[10.1029/2006JC003784](https://doi.org/10.1029/2006JC003784).
- Shellenbarger, G.G., S.A. Wright, and D.H. Schoellhamer. 2013. A sediment budget for the southern reach in San Francisco Bay, CA: implications for habitat restoration. *Marine Geology*. doi:[10.1016/j.margeo.2013.05.007](https://doi.org/10.1016/j.margeo.2013.05.007).
- Simpson, J.H., J. Brown, J. Matthews, and G. Allen. 1990. Tidal straining, density currents, and stirring in the control of estuarine stratification. *Estuaries* 13(2): 125–132.
- Sommerfield, C.K., and K.C. Wong. 2011. Mechanisms of sediment flux and turbidity maintenance in the Delaware Estuary. *Journal of Geophysical Research* 116(C01005). doi:[10.1029/2010JC006462](https://doi.org/10.1029/2010JC006462).
- Thompson, J.K., J.R. Koseff, S.G. Monismith, and L.V. Lucas. 2008. Shallow water processes govern system-wide phytoplankton dynamics: a field study. *Journal of Marine Systems* 74: 153–166. doi:[10.1016/j.marsys.2007.12.006](https://doi.org/10.1016/j.marsys.2007.12.006).
- Urick, R.J. 1967. *Principles of underwater sound for engineers*. New York: McGraw-Hill.
- Valle-Levinson, A., C. Reyes, and R. Sanay. 2003. Effects of bathymetry, friction, and rotation on estuary-ocean exchange. *Journal of Physical Oceanography* 33(11): 2375–2393.
- Wall, G., E. Nystrom, and S. Litten. 2006. Use of an ADCP to compute suspended-sediment discharge in the tidal Hudson River, New York. Scientific investigations report 2006-5055. Reston: U.S. Geological Survey.
- Walters, R.A. 1982. Low-frequency variations in sea level and currents in South San Francisco Bay. *Journal of Physical Oceanography* 12(7): 658–668.
- Walters, R.A., R.T. Cheng, and T.J. Conomos. 1985. Time scales of circulation and mixing processes of San Francisco Bay waters. In *Temporal dynamics of an estuary: San Francisco Bay*, chap 2, eds. J.E. Cloern and F.H. Nichols, 13–36. Dordrecht: W. Junk Publishers.
- Wong, K.-C. 1994. On the nature of transverse variability in a coastal plain estuary. *Journal of Geophysical Research* 99(C7): 14,209–14,222.